ARMA 19–1809

A Methodology to Measure Fracture Aperture Using A Consumer Grade Digital Camera

Villamor Lora R., Li B.Q., and Einstein H.H.
Massachusetts Institute of Technology, Cambridge, MA, USA

This paper was prepared for presentation at the 53rd US Rock Mechanics/Geomechanics Symposium held in New York, NY, USA, 23–26 June 2019. This paper was selected for presentation at the symposium by an ARMA Technical Program Committee based on a technical and critical review of the paper by a minimum of two technical reviewers. The material, as presented, does not necessarily reflect any position of ARMA, its officers, or members. Electronic reproduction, distribution, or storage of any part of this paper for commercial purposes without the written consent of ARMA is prohibited. Permission to reproduce in print is restricted to an abstract of not more than 200 words; illustrations may not be copied. The abstract must contain conspicuous acknowledgement of where and by whom the paper was presented.

ABSTRACT: Experimental studies on fracture flow processes are vital to understand the dependence of fracture permeability on various complex processes. A key parameter in such experiments is the fracture aperture, which can be determined using light transmission techniques when using transparent fracture models. For this, scientific-grade monochrome cameras are used to record light intensity under different conditions. The output data of scientific cameras is linearly related to the radiance scene, which allows one to do quantitative analysis using such data. On the contrary, consumer-grade digital (CGD) cameras usually output nonlinear color images (e.g. JPG or TIFF files), which are not suitable for most scientific uses. In this paper, we outline an image analysis procedure to use CGD cameras for light intensity measurements. We demonstrate that the direct use of raw data from such cameras is adequate for scientific quantification and prevents the introduction of artefacts from further image processing that usually occurs within the built-in software of most cameras.

List of Abbreviations
CCD - Charge-Couple Device (image sensor)
CFA - Color Filter Array
CGD - Consumer Grade Digital (camera)
CMOS - Complementary Metal-Oxide-Semiconductor (image sensor)
RGB - Red-Green-Blue
SGD - Scientific Grade Digital (camera)

1. INTRODUCTION

Experimental studies have greatly contributed to our understanding of the dependence of fracture permeability on various complex processes (e.g. fracture deformation, dissolution). Recently, universal scaling relationships between fracture stiffness and fluid flow have been proposed (Pyrak-Nolte and Nolte, 2016). Theoretical and numerical investigations have led to a number of models, for instance, for fracture deformation and closure (e.g. Kling et al., 2018), and corrections to the widely used Local Cubic Law (Brown, 1987). Yet, experimentation remains an essential part of fracture flow studies since it can validate the models, point out inconsistencies of the models, and reveal new physical aspects. Important challenges in experimental investigations of fracture flow are related to multiple processes occurring simultaneously, as well as specimen heterogeneity and test repeatability.

Systematic investigations require controlled variation of the geometric- and mechanical properties of the fractured specimens. Certainly, numerical simulations can address the above-mentioned issues. However, the validity of such simulations depends on a series of assumptions that not always hold. The use of fracture replica and fracture analogs presents a great advantage here, it provides the possibility of efficient specimen replication, so one can conduct systematic experimental investigations while controlling the geometric and material properties.

Furthermore, when such fracture -replicas and -analogs are fabricated using transparent materials, direct measurements of the fracture aperture field (Detwiler et al., 1999), flow (Nichol et al., 1999), and dissolution- (Detwiler, 2008) and transport- (Nowamooz et al., 2013; Lee et al., 2015) processes are also possible. The basics for such measurements rely on light transmission techniques (see Section 3), and in general, the experimental setup consists of (1) a diffuse light source, (2) a transparent fracture cell, and (3) a digital camera (Figure 1). The experimental procedures are as follows: at different times during the test, clear- or dyed-solutions are injected into the transparent fracture cell, and the transmitted light intensity is recorded by the camera. After image processing, these changes in the recorded light intensity can be related to flow velocities, variations

in the aperture, fluid saturations, and tracer concentrations.

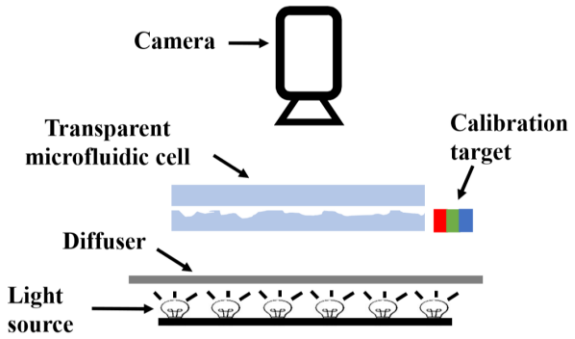

Fig. 1. Typical setup used in light transmission experiments. A digital camera records the light intensity transmitted through a transparent microfluidic cell. The light source must generate a uniform irradiance (hence the diffuser). A calibration target consisting of an object of known color is usually placed next to the cell to correct for white-balance and light-intensity fluctuations.

In light transmission experiments, light intensity is traditionally recorded using scientific grade digital (SGD) cameras, usually being monochrome Charge-Coupled Devices (CCD) (e.g. Detwiler et al., 1999). Such systems are quite popular for experiments with an intense imaging- component: they are easy to use, and the output is a linear representation of the scene radiance. On the other hand, consumer grade digital (CGD) cameras are present in most research laboratories, mostly for imaging of experimental setups, specimens, and other non-quantitative uses. However, CGD cameras do also have scientific-quantitative uses such as digital image correlation (Li and Einstein, 2017); and image processing of their sensor raw data enables one to use them as SGD cameras (Akkaynak et al., 2014; Sumner, 2014).

In this paper, we outline a procedure to use raw data from CGD cameras for light intensity measurements, and emphasize why this is necessary (Section 2). Then, we introduce the Beer-Lambert law, and present a study in which we measured aperture fields in transparent fracture cells using a CGD (Section 3). Note that a comparison between SGD vs. CGD cameras is beyond the scope of the present paper. We simply provide a methodology to conduct fracture aperture measurements with a CGD camera in the case a SGD one is not available.

1.1. Consumer Grade Digital (CGD) Cameras

One can find consumer grade digital cameras (also known as commercial off-the-shelf digital cameras) in nearly every single research laboratory. They have attractive pricing, high resolution, are widely available, and easy to use. However, they are not optimally designed for scientific data quantification (Akkaynak et al., 2014). CGD cameras incorporate built-in image processing software that makes photographs look aesthetically pleasing to the human eye and introduce non-linearities and compression artifacts that hinder their use as scientific instruments.

On the contrary, SGD cameras output intensity photographs (i.e. n x m x 1 arrays) that can be linearly related to the scene radiance, i.e. their output is a linear function of the recorded light intensity. Nevertheless, SGD tend to have lower resolution compared to CGD cameras, and are pricier: $4,000- $8,000 for SGD vs. $500- $1,500 for CGD (Spotimaging, 2019). It is therefore desirable to use CGD cameras for scientific data acquisition, particularly given the fact that their image sensors also produce linear outputs. However, access to this linear data requires specific image processing which will be detailed in this paper.

Digital cameras convert light waves into electric signals through their image sensors, or imagers. The two main technologies are (1) semiconductor charge-couple devices (CCD), and (2) active pixel sensors in a complementary metal-oxide-semiconductor (CMOS). Discussing the difference between the two technologies is beyond the scope of the present paper, but major differences reside in signal noise, light sensitivity, and power consumption. Note that CCD sensors are used in the higher-end cameras. For the purpose of this paper it is sufficient to know that both sensor types consist of a 2D array of millions of tiny cells that output the value of the light intensity that they receive. Each of these tiny cells is able to measure light intensity, with no color data. Such a sensor with no color filtering only outputs images in gray scale, also known as monochrome.

Fig. 2. Digital cameras convert light intensity into electrical signals through image sensors. Color separation is usually achieved using color filter arrays (CFA), which are mosaics of tiny color filters. The most common CFA is the Bayer filter with arrangements consisting of one red-, one blue-, and two green-pixels (the higher concentration of green pixels compared to red or blue is to emulate the human eye, which is more sensitive to green shades than red or blue). Depending on the camera model the Bayer mosaic may present 'GRGB', 'BGGR', 'RGBG' , or 'RGGB' arrangements (the 'RGGB' arrangement is shown in the figure).

Color, i.e. RGB (Red-Green-Blue), cameras work on the same principle as monochrome ones, but add one more step for color separation. The most common approach is called the Bayer filter mosaic, where each individual pixel is made sensitive to one color only (i.e. either red, green, or blue) using a color filter array (CFA) as illustrated in

Figure 2. Note that each pixel in any RGB digital image contains information on all the three colors, with the two missing intensities interpolated from the neighbors.

1.1.1 Image Acquisition with CGD Cameras

For both monochrome- and color- cameras, the raw data from the image sensor appear as linear intensity images (i.e. n x m x 1 arrays). In the case of monochrome SGD cameras, the raw data are the file output, and ready to be used for quantitative analyses. On the other hand, in the case of (color) CGD cameras the raw data undergo a series of nonlinear transformations and compressions within the built-in software of the camera, resulting in a JPG file. Therefore, if one intends to use a CGD camera for scientific data acquisition, it is necessary to access the raw data in the form of a RAW file.

RAW files contain the uncompressed information recorded by the sensor, along with meta-data generated at the time of the image capture (e.g. camera model, white balance, light sensitivity [i.e. ISO], shutter speed, etc.). Many CGD cameras allow one to save shots as RAW files, however they usually come in a proprietary format (e.g. Canon's .CR2), which often has an obscure structure and is not easy to read. Nevertheless, there exist open raw image formats such as the Adobe's Digital Negative (.DNG), to which many proprietary RAW formats can be converted. For further information about RAW files, see Sumner (2014).

So, the first step in our workflow requires the acquisition of the RAW file. Usually, this can be done through the camera settings (prior to the shot), and/or through the camera controlling software. In our case, we use *digiCamControl*™, an open-source camera control software that allows for real time viewing, among many other functions such as setting the exposure, ISO, focusing, white balance, RGB histogram analysis, time-lapse, etc.

2. DATA PROCESSING OF RAW IMAGES

As just mentioned, proprietary RAW files are difficult to read and process. Some versions of *Windows*™ can generate preview, even recent versions of *MATLAB*™ programming language (Mathworks, Inc. Natick, Massachusetts) can *import* them. However, most of the times one will be opening the embedded JPG file into the RAW and not the *raw data* file itself. For this reason, we recommend to convert the RAW file (in our case .CR2) to .DNG, e.g. by using the free Adobe DNG Converter™.

DNGs are *open* (non-proprietary) RAW formats that can be read and processed using third-party software. However, some transformations to the raw data are needed. The image processing detailed in this section is similar to the camera's built-in software, but in a controllable (known) manner (Figure 3).

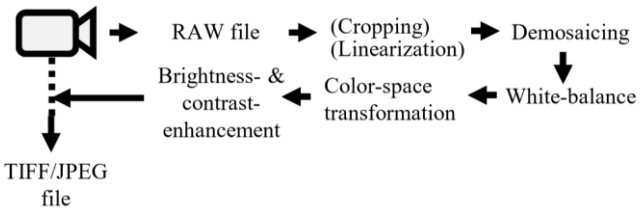

Fig. 3. Flowchart of image processing from raw data acquisition (image sensor) to a screen-displayable RGB image. Usually, the whole process happens *under-the-hood* within the camera's built-in software. Steps in parenthesis, ( ), are optional.

In general, before an image is ready to be displayed on a screen, the raw data from the sensor need to be (0) cropped, (1) linearized, (2) demosaiced, (3) white-balanced, (4) transformed to the expected color space, and (5) brightness- and contrast- enhanced as described below (Figures 3 and 4). In this section, we follow the steps detailed in Sumner's (2014) guide. A similar approach is shown in Akkaynak et al. (2014), along with some interesting applications. Since the procedure is extensively detailed in Sumner (2014), we limit ourselves to a structured overview of the process, with comments regarding the importance of each step, and which steps are unnecessary depending on the intended usage. We wrote our implementation of Sumner's (2014) guide into a single *MATLAB*™ function that can be downloaded at https://www.mathworks.com/matlabcentral/fileexchange/71420-dng-to-rgb-converter.

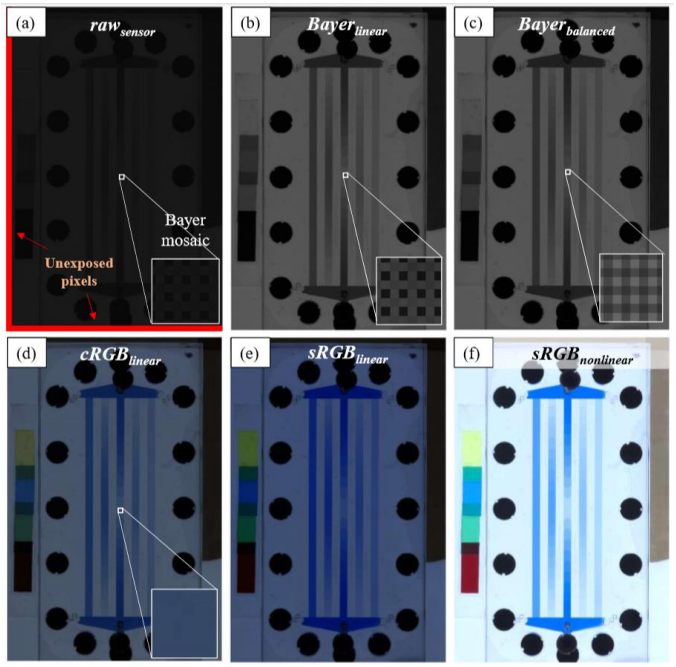

Fig. 4. Example of image processing from raw data acquisition (image sensor) to a screen-displayable RGB image. The image shown is a microfluidic cell used in the calibration of light-intensity vs. aperture gap (Figures 1 and 7). The different steps during image processing are: (a) Raw data from camera sensor, (b) Linear Bayer mosaic, (c) Linear Bayer mosaic + white-balanced, (d) Linear RGB [device-specific color space], (e) Linear RGB [device-independent color space], (f) Nonlinear RGB [brightness- + gamma- correction].

2.1. *Import Color Filter Array Image*

As noted before, the DNG file is mainly composed of two parts: (1) the intensity recorded by the image sensor (raw_{sensor}), and (2) meta-data with important information (*meta_data*), some of which we will detail later (e.g. presence of unexposed pixels, exposure time, color space). For further information regarding image formation principles, please refer to Akkaynak et al. (2014). For the purpose of this paper it is sufficient to know that raw_{sensor} is an intensity image (16bits, unsigned), which is a function of the source light (irradiance), the light reflected by the body (radiance), and the camera hardware (i.e. optics, spectral sensitivity of the Bayer filter and the sensor, and other electronics, e.g. Analog-Digital Converter). Therefore, two different cameras may output different raw_{sensor} images from the same scene. Moreover, the same camera may output slightly different raw_{sensor} from the same scene due to light source fluctuations, and/or sensor noise.

Figure 4a shows raw_{sensor} directly from the sensor, with an insert detail of the CFA. Note that the resolution of raw_{sensor} (i.e. the size of the nxmx1 array) may be larger than expected since it may include unexposed pixels. The physical location (i.e. coordinates) of these unexposed pixels can be found in *meta_data*. Note that each pixel of raw_{sensor} only contains information from one of the RGB channels (see Section 1.1). The two missing RGB values (channels) will be interpolated from the neighbors during the demosaicing (see Section 2.4).

2.2. *Linearization*

Although the output from the camera imager is linear, some cameras may apply a nonlinear transformation before generating the raw_{sensor} file (Sumner, 2014). If so, a linearization table can be found in *meta_data* so it can be reversed (if there is no such table, the image is linear).

Prior to white balancing and demosaicing there is one more step. We previously noted that raw_{sensor} is a 16-bit unsigned intensity image (i.e. intensity values range from 0 to 2^{16}-1). However, the imager of our camera may have a lower bit resolution (in our case it is 14bit). Therefore, the expected black level may not be 0, and similarly, the expected pixel saturation may not be 65,536 (i.e. 2^{16} - 1).

Using the black- and saturation- levels specified in *meta_data*, we perform an affine transformation to raw_{sensor} to normalize it to the range [0, 1] as follows (see also *'RGB Equalization'* in Akkaynak et al. (2014));

$$Bayer_{linear} = \frac{raw_{sensor} - black_{level}}{saturation_{level} - black_{level}} \quad (1)$$

Note that due to sensor noise, there may be values beyond this range, and therefore, such values need to be truncated to 0 and 1. The resulting array is a linear Bayer mosaic, i.e. the $Bayer_{linear}$ (Figure 4b).

2.3. *White Balancing*

We previously noted that the color recorded by a camera sensor is a combination of the irradiance (illuminating light) and the radiance (reflected light from the body). As a result, fluctuations in the light source will affect the camera readings. While the human eye can discount small changes in the ambient light through chromatic adaptation, cameras cannot (Akkaynak et al., 2014). Therefore, one needs to compensate for the color of the irradiance, i.e. we need to white-balance the image. In other words, we need to compensate the relative RGB values of each pixel, so a *white* pixel looks *white*. Fortunately, the same correction (i.e. same factors) is used in every pixel.

In order to do this, we need to either (i) use a calibration target, or (ii) measure the ambient light spectrum (Akkaynak et al., 2014). A calibration target is basically a reference with a known color, i.e. something with known RGB values. Once we know the *true* RGB values of a pixel we can adjust the measured RGB values until they match each other.

There are different algorithms one can use, including the chromatic adaptation transform or the RGB equalization (both described in Akkaynak et al., 2014). Sumner (2014), on the other hand, reduces the problem to simply finding the relative scaling of the red- and blue- channels to the green one ($WB_{multipliers}$). For example, if the RGB values of a pixel is *truly* white, then the two $WB_{multipliers}$ should equalize the RGB values (Figure 5).

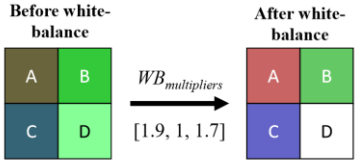

Pixel	R	G	B
A	0.4 (0.8)	0.4(0.4)	0.2(0.4)
B	0.2(0.4)	0.8(0.8)	0.2(0.4)
C	0.2(0.4)	0.4(0.4)	0.5(0.8)
D	0.5(1.0)	1.0(1.0)	0.6(1.0)

RGB values ~ Before (After)

Fig. 5. White-balance example. The table contains the RGB values of the group of four pixels before and (after) the white-balance. If one knows the pixel 'D' is white (i.e. RGB = [1,1,1]), the $WB_{multipliers}$ are such that [0.5, 1.0, 0.6] is transformed to [1.0, 1.0, 1.0].

The trick here is to find these $WB_{multipliers}$. One option would be to use a calibration target where these can be measured. Another, is to use the $WB_{multipliers}$ values present in the *meta_data*. However, note that these are not the true $WB_{multipliers}$ but an approximation from the camera or the user settings.

The output is a linear Bayer mosaic that is white-balanced, i.e. $Bayer_{balanced}$ (Figure 4c). But note that it may be no longer normalized to [0, 1]. $WB_{multipliers}$ may have

caused the maximum value of $Bayer_{balanced}$ to be beyond 1. We have the option of either (i) scaling back everything to [0, 1], or (ii) truncating the values beyond 1. In other words, we can choose between the (i) loss of an absolute scale, or (ii) information loss. We implement the latter one.

2.4. *Demosaicing*

So far, the image map is a Bayer mosaic image which is an intensity image, i.e. a n x m x 1 array. The demosaicing algorithm will generate a full RGB image which is a n x m x 3 array. For each pixel, the algorithm will interpolate the two missing RGB values.

There are different demosaicing algorithms. Some of them, e.g. the bilinear interpolation, determine the missing values for a given RGB channel from the known values of that channel. Others, like the gradient-corrected bilinear interpolated approach (Malvar et al., 2004) employ additional information from other color channels (Figure 6). The latter usually yield better results compared to bilinear, but may introduce artefacts, especially when dealing with dyes that are transparent to certain colors. Moreover, the relative order between the white balancing- and demosaicing- algorithms may affect the result since the correction for changes in intensity gradients uses other known colors, which may have been affected by the $WB_{multipliers}$.

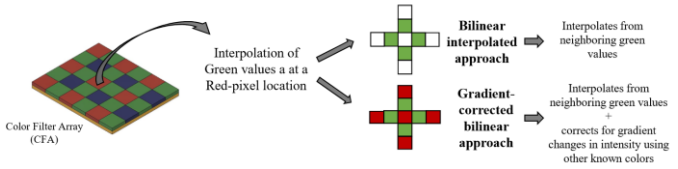

Fig. 6. Demosaicing principles for two different algorithms. For a given RGB channel the bilinear approach only uses known values for this channel. On the other hand, the gradient-corrected bilinear approach also uses information from other color channels. We implement the latter.

In addition, recall that the recorded RGB values are device-specific. Different cameras use different CFAs, being sensitive to different regions of the light spectrum. Therefore, at the end of the demosaicing step, one will have generated a linear RGB image in the camera-specific color space, the $cRGB_{linear}$ image (Figure 4d). This is enough if one intends to use the camera as a scientific instrument because, like any other sensor, this output from the camera can be calibrated against a reference. And for this reason, $cRGB_{linear}$ images will be used in our analysis.

2.5. *Color Space Conversion and Brightness and Gamma Correction*

The linear transformation required to convert an image from a device-specific to a device-independent color space is called color space transformation ($cRGB_{linear}$ → $sRGB_{linear}$). This may be important if work repeatability is required. Details for this transformation can be found in Akkaynak et al. (2014) and Sumner (2014). The resulting photograph is a linear RGB image that is a device-independent version of the raw camera output, i.e. the $sRGB_{linear}$ image (Figure 4e), for which colors do not depend on a specific CFA filter combination. Note that after this operation it is possible that some RGB fall beyond the [0, 1] range, with the consequent information loss (see Section 3.3.3).

Nevertheless, the resulting image might not be yet aesthetically pleasant. Usually there is one last step involving brightness- and gamma- (i.e. nonlinear transformation) corrections. These are highly subjective and the resulting image, the $sRGB_{nonlinear}$, must not be used for scientific purposes since it will be highly nonlinear.

As the reader may have noted not all the steps detailed in this section are necessary to be able to measure light intensity with a CGD camera. For instance, accessing the raw_{sensor} data plus demosaicing is enough for sensor calibration if one only needs one of the RGB channels. However, we provided the full workflow to illustrate why image processing of the raw data is necessary, which are the options, and why is not a good idea to use the JPG or TIFF files since these are $sRGB_{nonlinear}$ images, i.e. they use a nonlinear scale which is not appropriate for data calculations.

3. FRACTURE APERTURE MEASUREMENTS USING LIGHT TRANSMISSION TECHNIQUES

In this section we present the theoretical background for aperture measurements using light transmission techniques (the Beer-Lambert law). We also describe a simple setup using a LED panel, a microfluid cell, and a CGD camera. Then we apply the image processing workflow described in Section 2 to demonstrate how fracture aperture measurements can be made using a CGD camera.

3.1. *Theory: Beer-Lambert Law*

As first proposed by Glass et al. (1991), aperture fields in microfluidic cells can be measured using light absorption theory, which is described by the Beer-Lambert Law (Detwiler et al., 2000). This empirical relationship relates monochrome-light absorption to material properties of the light-transmitting media (e.g. liquid, gas). For the case of solute dissolved in a liquid, the transmitted light intensity measured at a given point (x, y) is given by:

$$I_C(x,y) = I_0(x,y)10^{-\varepsilon C(x,y)h(x,y)} = I_0(x,y)10^{-A(x,y)} \quad (2)$$

where I_C and I_0 are light intensities measured with- and without the solute present in the solution, respectively (Figures 8a,b). The product εCh is the absorbance (A), with ε and C being the dye -absorptivity (a solute property) and -concentration; and h is the solution thickness, i.e. in our case the local fracture aperture. Note

that I_0 is not the irradiance (incident monochrome-light intensity) but the radiance from the cell filled with clear solution (C = 0), i.e. I_0 already accounts for the absorbance of the solvent and the transparent cell.

Equation 2 describes the attenuation of light intensity as it travels through a solution as a function of the dye concentration and the distance travelled. Once the dye absorptivity is known (e.g. Norwamooz et al., 2013), the aperture field can be determined by measuring the absorbance (i.e. $A(x,y) = log_{10}[I_0(x,y)/I_C(x,y)]$) at a given dye concentration. Moreover, Glass et al. (1991) showed that the aperture field can also be determined without measuring ε but the mean aperture of the fracture, $\langle h \rangle$, instead (Detwiler et al. 1999):

$$h(x,y) = A(x,y)\langle h \rangle / \langle A \rangle \quad (3)$$

Finally, recall that the Beer-Lambert law relies on the assumption of monochromatic light irradiance. In the case of polychromatic light source, Equation 2 is only approximate and non-linearities may arise since dye absorptivity is a function of the wavelength. Such non-linearities are found to increase with increasing dye concentration (Detwiler et al., 2000).

3.2. Methods

The experimental setup was shown in Figure 1 and comprises (1) a diffuse light source, (2) a transparent fracture cell, and (3) a digital camera. The diffused light source consists of an LED panel (Autograph™ 930 LX LightPad™) connected to a stable DC power supply (Keysight™ E3630A) in order to minimize voltage and current fluctuations.

The transparent cell is made of two 1/2"-thick acrylic plates screwed to each other. Five different height profiles were CNC-machined onto one of the plates as shown in Figure 7. Each one of these profiles consists of a single channel with either constant- (AA' and EE') or variable- (BB', CC' and DD') depth. For the sake of simplicity in this study, only the variable depth of the central profile will be used to determine the light intensity vs. depth calibration.

We used a CGD camera (Canon™ EOS 6D) with a 14bit CMOS trichromatic sensor, and a 100 mm f/2.8 macro lens. The camera was computer-operated using DigiCamControl™ software. We took pictures with lens aperture of f/32, ISO-100, and exposure time equal to 1.3 s. The smallest lens aperture available (i.e. f/32) was selected in order to maximize the depth of field, and therefore minimize possible errors due to misalignments in the perpendicularity between the camera and the transparent cell. Similarly, the smallest ISO available (i.e. ISO-100) was chosen to minimize noise (i.e. graininess). Finally, after setting both lens aperture and ISO, the exposure time was selected to maximize the usable dynamic range of the camera (see Figure 9).

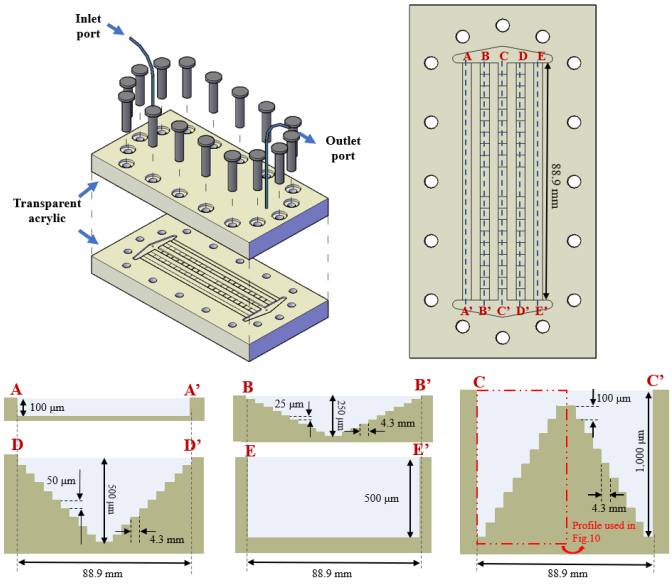

Fig. 7. Transparent microfluidic cell for light intensity vs. height calibration. Five different stepped profiles were CNC-machined onto the bottom plate of the cell. Details for each profile (i.e. step -height and -length, maximum depth, and total length) are shown in the five cross sections (AA', BB', CC', DD' and EE').

The solute is a blue-powder (Alfa Aesar™ Brilliant Blue G, ultrapure) dissolved in distilled water. This dye, also known as Coomassie Brilliant Blue G-250, is light-absorbing (red- and green- wavelengths, hence its blue color) and highly soluble in water (50 mg/mL). It produces dark blue solutions even at low concentrations (< 1mg/mL), which is advantageous for imaging small fracture apertures. Recall that CGD cameras are more sensitive to green shades compared to red or blue (Figure 2). Therefore, a dye which does absorb wavelengths within the green range is preferred.

In this study, we measured fracture apertures using six different solute concentrations (0, 1/32, 1/16, 1/8, 1/4 and 1/2 g/L). Prior the injection of each dye solution, the cell was flushed with air to avoid mixing with the previous solution. We then injected the new target concentration solution to achieve a homogeneous target concentration.

Finally, ten pictures were taken at each concentration, and then averaged to minimize noise. A group of white pixels were used as a calibration target (Figure 8) for light intensity fluctuations as discussed in Section 3.3.1.

3.3. Results and Discussion

3.3.1 Image Processing and White Balance

In the following analysis, only the $cRGB_{linear}$ images were considered. These were developed using the $WB_{multipliers}$, and the linear transformation factors embedded in the *meta_data* of the DNG file. Nevertheless, a subsequent analysis of a group of white pixels indicated that LED panel fluctuations resulted in variations of light intensity up to 8% among the images taken at the same exposure

time. These fluctuations were corrected using the first image as a reference.

3.3.2 Trichromatic Analysis

As noted in Section 1.1, a major difference between CGD- and monochrome SGD- cameras is the ability of the former to capture trichromatic (i.e. RGB) images. Notwithstanding that raw RGB images require more image processing, trichromatic images may have some advantages. First, they provide filtering into three different color channels (i.e. RGB) due to the CFA in the imager. Some studies using monochrome cameras (e.g. Detwiler et al., 1999) actually use a monochrome filter before the camera objective in order to approximate the monochrome-light requirement of the Beer-Lambert Law

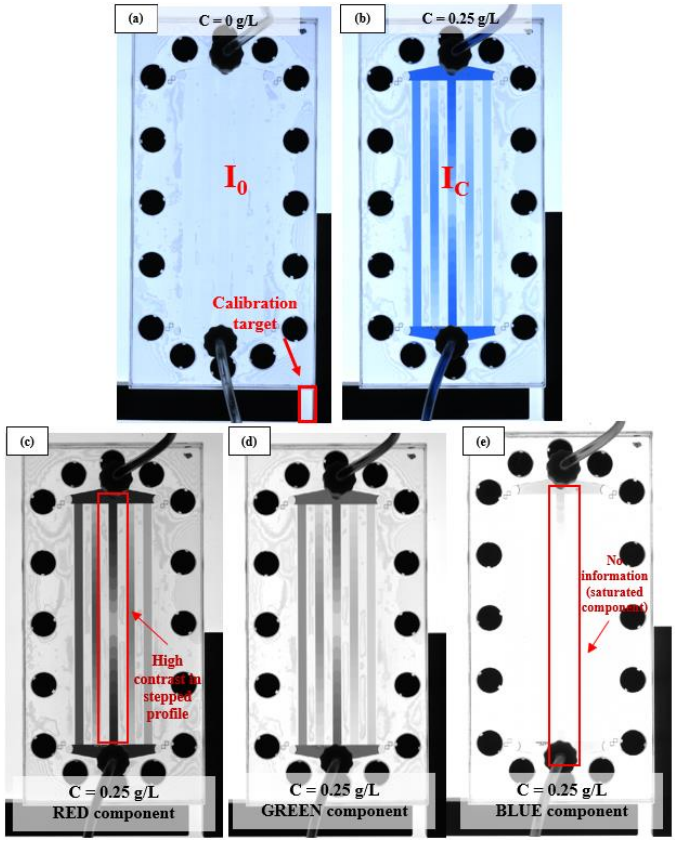

Fig. 8. *cRGBlinear*: Calibration cell filled with (a) clear- and (b) dyed- solutions. (c-e) RGB components of image (b). Lens aperture f/32, ISO-100, Shutter speed 1.3 s, Dye concentration = 0.25 g/L. Note the calibration target at the bottom right of the cell.

Figure 8 compares RGB images of the calibration cell filled with (a) clear- and (b) dyed- solutions (i.e. I_0 and I_C). Then, the I_0 RGB image is separated into R-, G-, and B- channels. Since the dye is blue, the B channel will be *high*, in terms of intensity, while the others (R and G) will be *low*. Recall that when one sees an object of a specific color it is because it reflects that specific range of wavelengths, absorbing the others.

Moreover, recall that Figure 8 is in the camera-specific color space (due to the camera's specific CFA). The relative intensity among RGB channels may be different if one considers another color space, e.g. the device-independent color space. However, one must be careful when performing linear transformations from the device-specific to device-independent color spaces (see Section 2.5), as some RGB values may fall beyond the [0, 1] range with the consequent information loss.

By preliminary observation of Figure 8 one may notice that some RGB channels contain more information than others (e.g. height steps are more obvious in Figure 8c than Figure 8e, which is almost saturated). Figure 9 shows the light intensity along the central profile (CC' in Figure 7) of the calibration cell under clear water- (I_0) and dye- (I_C) conditions for the three RGB channels. Note that although one may see the steps in all the three channels, what is informative is the I_0/I_C ratio. Due to low contrast, the blue channel is much noisier than the other two, and therefore, only R- and G- channels will be considered in the rest of the analysis. Moreover, Figures 9(a, b) compare the light intensity profiles measured at two different shutter speeds (0.6 vs. 1.3 s). This illustrates how the shutter speed maximizes the usable dynamic range of the camera. In this study, the shutter speed was adjusted based on the R- and G- channels (i.e. the ones considered in the following analysis).

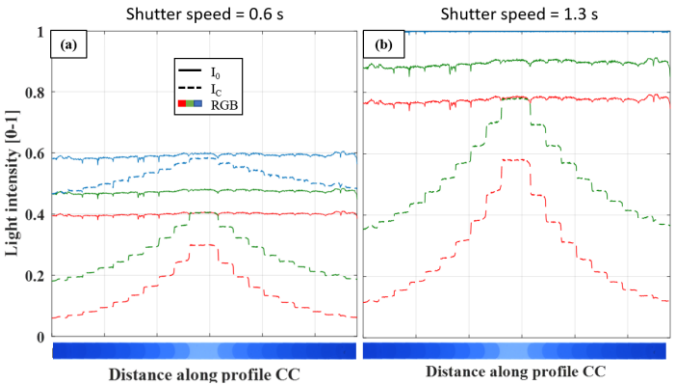

Fig. 9. *cRGB$_{linear}$*. Light intensity along the central profile (CC' in Figure 7) of the calibration cell under clear- (solid lines) and dyed- (dashed lines) solution conditions. Each RGB channel is plotted separately. Note the R- and G- channels show high I_0/I_C contrast (i.e. large relative differences between I_0 and I_C lines). Lens aperture f/32, ISO-100, Dye concentration = 0.25 g/L. Shutter speed equal to (a) 0.6 s and (b) 1.3 s. Note how by adjusting the shutter speed one can maximize the usable dynamic range of the camera.

3.3.3 Calibration Curve and Effect of Dye Concentration

After light source fluctuations have been corrected (see Section 3.3.1), the light intensity profiles, such as the ones shown in Figure 9b, can be used to generate *light intensity* vs. *fracture aperture* calibration curves (Figure 10b). To generate these curves, we first normalize the light intensities at any given concentration by the light intensity at zero concentration (i.e. I_0/I_C) as shown in Figure 10a.

Then, the individual normalized intensities (i.e. steps in Figure 10a) are related to their corresponding height-aperture gap, and used to determine the I_0/I_C *vs. h* calibration curves (Figure 10b).

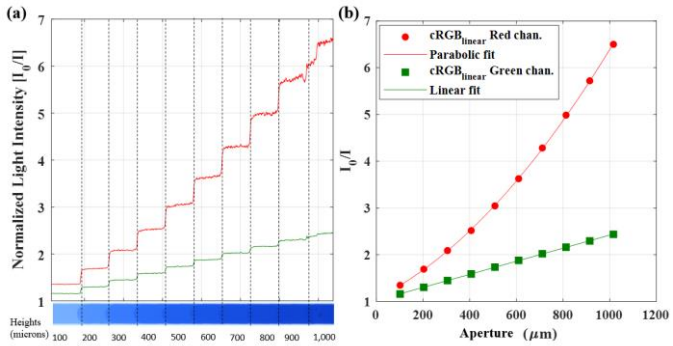

Fig. 10. (a) Normalized light intensity along the central profile of the calibration cell (see profile CC' in Figure 7). The x-axis corresponds to the distance along the stepped profiles, with each step corresponding to a specific height. Red- and green- curves correspond to the red- and green- channels, respectively. (b) I_0/I_C vs. *height* calibration curve for the red- and green- channels. Dye concentration = 0.25 g/L. Note that we use light intensities from the green- and red- channels of the $cRGB_{linear}$ images only.

These steps can be repeated for each investigated dye concentration (i.e. 1/32, 1/16, 1/8, 1/4 and 1/2 g/L). Figures 11a and 11d show the I_0/I_C *vs. h* calibration curves at a range of concentrations, for the red- and green- channels, respectively. Specifically, we note that the I_0/I_c *vs. height* curves plot almost linearly on the green channel (Figure 11d) while I_0/I_c *vs. height* curves derived from the red channel (Figure 11a) seem to transition from linear- to quadratic- to cubic- trends. This different behavior between red- and green- channels may be a result of the different absorption properties at different wavelengths (Detwiler at al., 1999).

As discussed in Section 3.1, the Beer-Lambert law predicts a semilogarithmic relation between *normalized light intensity* (I_0/I_c) and *height*. Figures 11b and 11e are plotted in this manner, and we can see that the $log_{10}[I_0/I_C]$ (i.e. the *Absorbance)* vs. *height* relation is indeed linear at low concentrations. However, we observe that at concentrations above 1/8 g/L, the linear relation no longer holds. Nonlinearity at high concentrations has been previously reported (e.g. Detwiler et al. 1999), and is usually attributed to the non-fulfilment of the monochromatic light source requirement (see Section 3.1). In our case, curves in Figures 11(b, e) show a transition from linear to quadratic, suggesting that the observed non-linear absorbance could be accounted for by a function of the following form:

$$log_{10}\left[\frac{I_0(x,y)}{I_c(x,y)}\right] = f\{C(x,y)\}\,h(x,y)^2 + g\{C(x,y)\}\,h(x,y) \quad (4)$$

where $f\{C(x,y)\}$ and are $g\{C(x,y)\}$ functions of concentration. Figures 11(c ,d) show examples of data fitting using Equation 4 with $f=\{a\,C(x,y)^2 + b\,C(x,y)\}$ and $g=\{d\,C(x,y)\}$, where a, b, and d are fitting parameters. Note that no determination of the dye absorptivity was attempted (ε is embedded in the fitting parameters a, b, d).

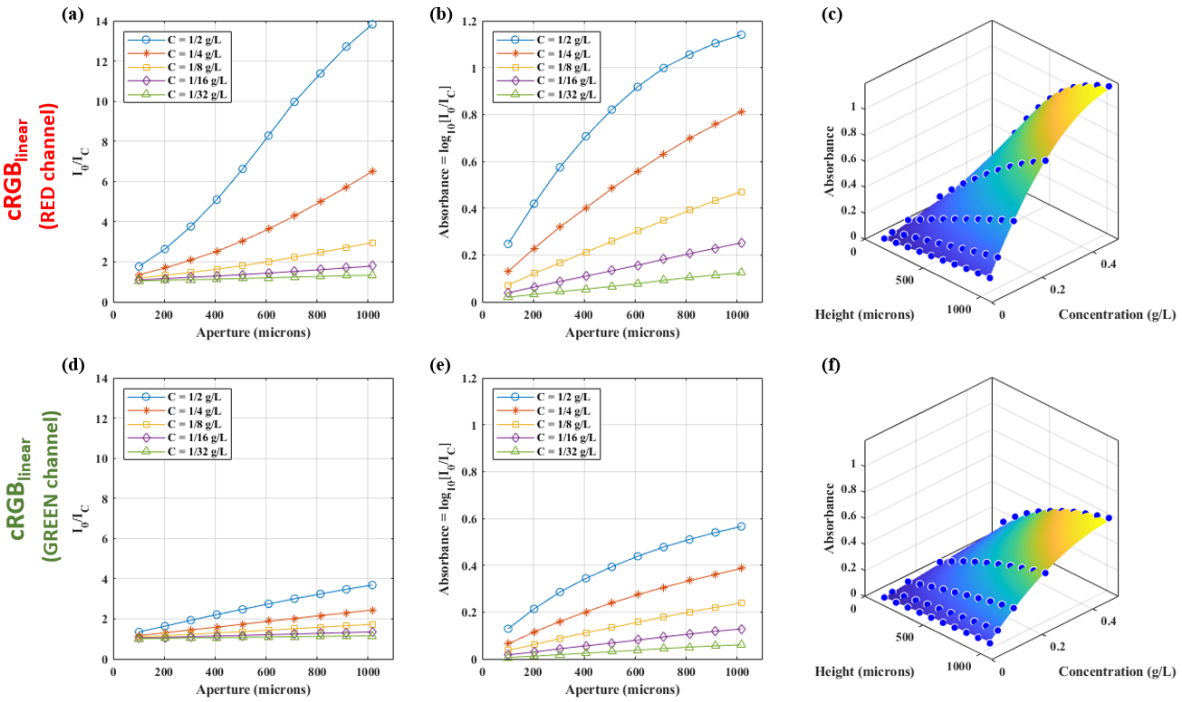

Fig. 11. Normalized light intensities as a function of aperture height and dye concentration. I0/IC vs. height curves for the (a) red- and (d) green- channels. *Absorbance* ($log_{10}[I_0/I_C]$) vs. *height* curves for the (b) red- and (e) green- channels. Absorbance vs. height vs. concentration curves for the (c) red- and (f) green- channels. Data from $cRGB_{linear}$ images.

The goodness of fit reveals that the chosen model is able to fit our laboratory data, with R^2 equal to 0.999 and 0.996 for the red- and green- channels, respectively. We have confidence that the nonlinearities shown in Figures 11(b, e) are not artefacts from the demosaicing algorithm or the white balance corrections. To demonstrate this, we repeated the analysis above with the $Bayer_{linear}$ images and we obtained the same results. Finally, we repeated the analysis once more with $sRGB_{linear}$ images, and these resulted in higher nonlinearities and information loss (e.g. some pixels in the Red channel fall below [0,1]). Therefore, $sRGB_{linear}$ images are not recommended for this type of light intensity measurements

4. CONCLUSIONS AND COMMENTS

In this paper we outline a procedure to use raw data from CGD cameras for light intensity measurements. We illustrate how different stages during image processing enhance- and hinder the use of CGD cameras as scientific instruments.

A study where the microfluidic cell aperture was measured as a function of light intensity was also presented. Both the setup and theoretical background were discussed, showing the advantages and drawbacks of trichromatic CGD cameras. Experimental results show that the direct use of raw- (i.e. $Bayer_{linear}$ images) and low-processed data (i.e. $cRGB_{linear}$ images) is adequate and prevents the introduction of artefacts from further image processing.

For the specific -equipment and -experimental conditions used in this study (i.e. the dye and camera model with a specific CFA sensitivity), we obtained non-linear absorbance vs. height curves at high dye concentrations (differently from what is predicted by the Beer-Lambert law). This may be due to the nonlinear absorbance caused by our polychromatic light source. However, such curves were basic first- and second- order polynomials, and are simple to implement in the laboratory.

Finally, recall that previous studies have exclusively used monochrome cameras for aperture field measurements, and such instruments have proved to be very effective. However, we have shown that aperture field determinations are also possible with CGD cameras. In addition, there might be some other advantages of using a trichromatic camera. For instance, although not investigated in the present paper, it may be possible that different color dyes can be selected such they match the filters of the CFA. In such a case, individual RGB channels are sensitive to an individual dye only. This may be of interest when imaging mixing processes or multiphase flow. Moreover, note that a direct comparison between SGD vs. CGD cameras was not attempted. We leave that as an open question for future studies.

ACKNOWLEDGEMENTS

Financial support for this research was provided by ADNOC under the Research Project ID:015-RCM-2015 “Hydraulic Fracturing Simulation Modeling with Emphasis on Stress Dependent Conductivity”.

REFERENCES

1. Akkaynak, D., Treibitz, T., Xiao, B., Gürkan, U. A., Allen, J. J., Demirci, U., & Hanlon, R. T. 2014. Use of commercial off-the-shelf digital cameras for scientific data acquisition and scene-specific color calibration. *Journal of the Optical Society of America A*, 31(2), 312.
2. Brown, S. R. 1987. Fluid Flow Through Rock Joints: The Effect of Surface Roughness. *Journal of Geophysical Research*, *92*(B2), 1337–1347.
3. Detwiler, R. L., Pringle, S. E., & Glass, R. J. 1999. Measurement of Fracture Aperture Fields Using Transmitted Light: An Evaluation of Measurement Errors and Their Influence on Simulations of Flow and Transport Through a Single Fracture. *Water Resour. Res.*, *35*(9), 2605–2617.
4. Detwiler, R.L., Rajaram, H., & Glass, R.J. 2000. Solute transport in variable-aperture fractures: An investigation of the relative importance of Taylor dispersion and macrodispersion. *Water Resour. Res.*, *36*(7), 1611–1625.
5. Detwiler, R. L. 2008. Experimental observations of deformation caused by mineral dissolution in variable-aperture fractures. *Journal of Geophysical Research*, *113*(June), 1–12.
6. Glass, R.J., Nicholl, M.J., & Thompson, M.E. 1991. Comparison of measured and calculated permeability for a saturated, rough-walled fracture. *Eos Trans, AGU, 72(44), Fall Meet. Suppl., 2016*
7. Kling, T., Vogler, D., Pastewka, L., Amann, F., & Blum, P. 2018. Numerical Simulations and Validation of Contact Mechanics in a Granodiorite Fracture. *Rock Mechanics and Rock Engineering*, *51*(9), 2805–2824.
8. Lee, S. H., Yeo, I. W., Lee, K. K., & Detwiler, R. L. (2015). Tail shortening with developing eddies in a rough-walled rock fracture. *Geophysical Research Letters*, *42*(15), 6340–6347.
9. Li, B.Q. and Einstein, H.H 2017. Comparison of Visual and Acoustic Emission Observations in a Four Point Bending Experiment on Barre Granite. *Rock Mech Rock Eng.* 50: 2277.
10. Malvar, H. S., He, L. W., & Cutler, R. 2004. High-quality linear interpolation for demosaicing of Bayer-patterned color images. In *2004 IEEE International Conference on Acoustics, Speech, and Signal Processing* (Vol. 3, pp. iii-485). IEEE
11. Nowamooz, A., Radilla, G., & Fourar, M. 2013. Non-Fickian Transport in Transparent Replicas of Rough-Walled Rock Fractures. *Transport in porous media*, 98(3), 651–682.

12. Pyrak-Nolte, L. J., & Nolte, D. D. (2016). Approaching a universal scaling relationship between fracture stiffness and fluid flow. *Nature Communications*, *7*, 10663.

13. Spotimaging. Consumer Digital Cameras for Microscopy Imaging. Retrieved February 15, 2019 from http://www.spotimaging.com/resources/white-papers/consumer-digital-camera-microscopy-imaging/

14. Sumner, R. (2014). Processing raw images in MATLAB. *Department of Electrical Engineering, University of California Santa Cruz*.